Wavelength Jumps and Multimode Instabilities in Integrated Master Oscillator Power Amplifiers at 1.5 μm: Experiments and Theory

Antonio Pérez-Serrano, Mariafernanda Vilera, Julien Javaloyes, Jose Manuel G. Tijero, Ignacio Esquivias, and Salvador Balle

***Abstract*—We analyze the large (>10 nm) and abrupt jumps in emission wavelength, together with the multimode instabilities associated with them, which are observed in monolithically integrated master oscillator power amplifiers emitting at 1.5 μm. The physical origin of such phenomena is investigated in the framework of a travelling-wave model which phenomenologically incorporates thermal effects via self and cross-heating of the different sections of the device. The occurrence of the wavelength jumps and the instabilities as a function of the injected currents in the two sections is interpreted in terms of a thermally tuned competition between the modes of the master oscillator and the compound cavity modes.**

***Index Terms*—High power semiconductor lasers, master oscillator power amplifier, multimode dynamics, laser theory, compound cavity effects, thermal effects.**

I. Introduction

MONOLITHICALLY integrated master oscillator power amplifiers (MOPAs) are high-brightness semiconductor lasers that have the potential to be modulated at high speed, which makes them attractive sources for applications such as LIDAR, free space optical communications, and laser projection displays. An integrated MOPA usually consists of two sections: an index guided single lateral mode waveguide section acting as master oscillator (MO), and a power amplifier (PA). Normally, the MO is either a distributed Bragg reflector (DBR) or a distributed feedback (DFB) laser, while the PA is a gain guided tapered section with an antireflection (AR) coated output facet. Sensible progress in the performance of MOPAs has been achieved in last years. For monolithically integrated MOPAs at 1064 nm, 12 W output power in continuous-wave (CW) regime has been demonstrated, and also pulse generation with 42 W peak power and 84 ps pulse width [1]. At 1.5 μm, commercial devices delivering 1.6 W under CW injection have been gain switched to deliver 100 ps pulses with peak power up to 2.7 W at 1 GHz [2].

In a MOPA working in ideal conditions, the single-mode generated by the MO is amplified by the PA section keeping its initial beam quality. However, it is known that even when driven in the CW regime, a small residual reflectance of the MOPA front facet may induce a variety of emission instabilities for specific injection conditions [3], [4]. These instabilities manifest for instance in the appearance of ripples in the power-current (P-I) curves, arising as a consequence of the coupling between the modes of the full MOPA cavity and the MO modes [5]. Another manifestation is the appearance of self-pulsations in the optical power, which have been attributed either to longitudinal mode beating [2] or to the undamping of the relaxation oscillations (ROs) at a few GHz [3]. These instabilities in the CW regime are expected to impact the MOPA operation in direct modulation, thus jeopardizing the potential of these devices for applications requiring such modulation format. Therefore, a detailed understanding from both the experimental and the theoretical point of view of the physical mechanisms involved in the instabilities is of primary interest for the enlightening of the actual potential of these devices.

We have recently reported a systematic experimental study of the emission instabilities occurring in 1.5 μm integrated MOPAs under a wide range of CW injection conditions [4]. The explored injection conditions included a continuous variation of the PA section current for several fixed values of the MO current. In addition to other previously reported instabilities, our study revealed a different kind of instability that involves large (>10 nm) and sudden jumps in the emission wavelength of the MOPA [2], [4]. The instability occurs for low currents in the MO section, i.e., when the MOPA is close to threshold, and it appears and disappears in a quasi-periodic way as a function of the CW current in the PA section.

Different simulation models have included coupled cavity effects in the investigation of the dynamics of high power MOPAs under CW injection [6]. The experimental results have been

successfully reproduced when thermal effects were properly accounted [5]. It has been demonstrated that the effect of self- and cross-heating of the two MOPA sections on the refractive index thermal changes, and thus on the coupled cavity modal dynamics, accounts for the periodic mode hoping and the ripples appearing in the P-I characteristics [7].

In this paper, we use a conveniently adapted 1-D travelling-wave model (TWM) [8] for the theoretical analysis of the origin and characteristics of the instabilities arising as a function of the PA current, for several fixed values of the MO currents in these devices. A full description of the MOPA dynamics requires at least a 2-D spatial model [5], [9] in order to address the possible filamentation in the PA section which is out of the scope of this paper. Our goal is to reproduce the experimental results and gain some insight using the simplest model possible. We show that 2-D effects are irrelevant in the observed dynamics due to its longitudinal and thermal character, obtaining a good qualitative agreement between the experiments and the 1-D TWM. Our analysis indicates that the dominant effect at the root of this instability is the drift of the cavity modes over the modulated loss spectrum created by the compound cavity effects arising from the effective reflectivity of the output facet. Moreover than carrier-induced index changes, temperature changes lead to modal drifts that change the net modal gain. The thermal self- and cross-heating in each section shift the modes away from the minimum of the losses of the DFB in the MO section. As a consequence, the modes around the gain peak of the PA section may prevail during some current interval, until the modes close to the Bragg wavelength take over again.

In Section II, the relevant details of the device, the experimental setup, and the main experimental results are briefly summarized. Section III is devoted to the description of the theoretical model and to show the results of performing the threshold analysis of the MOPA. The numerical results of the MOPA dynamics above threshold are described in Section IV. Finally, a summary of the conclusion is given in Section V.

II. Experimental Characterization

A detailed description of the investigated devices and of the experimental setup has been reported elsewhere [4] and therefore only the most important features are repeated here. We used commercial MOPAs with emission wavelength close to 1550 nm (QPC 4715-0000). The lengths of the MO and PA sections were around 0.9 and 1.6 mm, respectively. Fig. 1(a) shows an schematics of the device geometry. Device characterization was performed at 25 °C. It included, as a function of the CW MO and PA currents, the total power measured with a thermal detector, the optical spectra measured with a 0.05 nm optical spectrum analyzer, and the electrical spectra measured with a high speed photodiode and a 44 GHz electrical spectrum analyzer. The experimental setup used to record the optical and RF spectra of the devices is described in Fig. 1(b).

In [4] we presented with detail the measured emission characteristics of this MOPA under different injection conditions. Here we remark the most interesting features to be compared with the theoretical results. The output power, the optical and RF spectra of the MOPA for different values of the current in

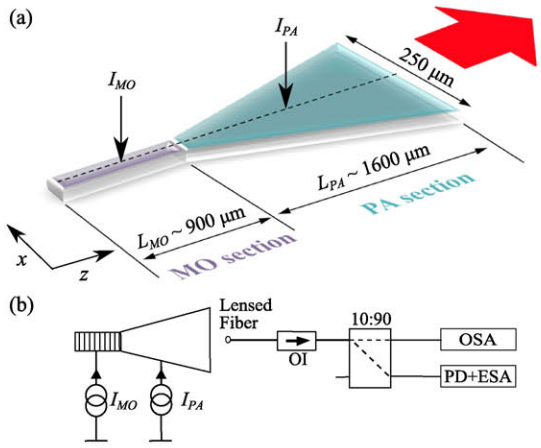

Fig. 1. (a) Schematics of the MOPA device composed by a DFB laser (MO section) and a gain guided flared amplifier (PA section). (b) Experimental setup for acquisition of the optical and RF spectra: optical isolator (OI), optical spectrum analyzer (OSA), photodetector (PD) and electrical spectrum analyzer (ESA).

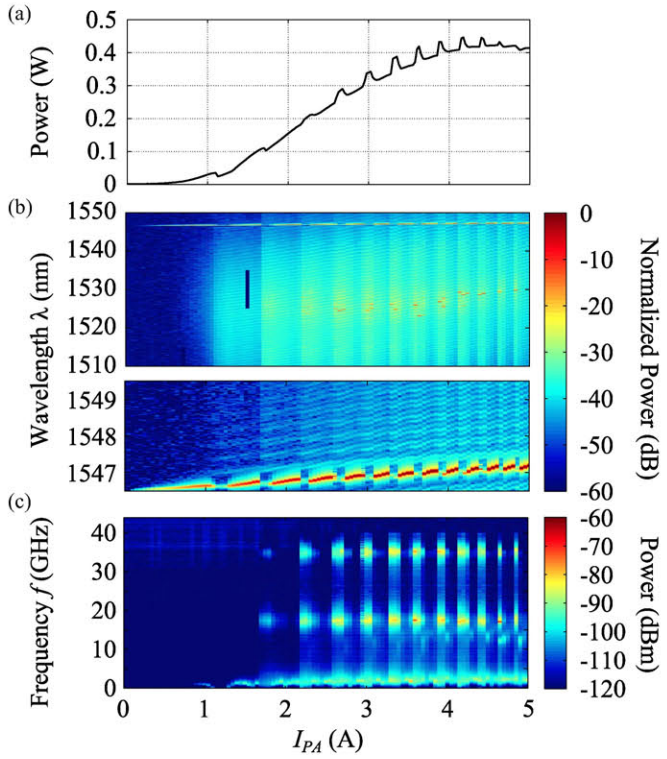

Fig. 2. Experimental characterization: (a) P-I characteristics for $I_{MO} = 30\,\mathrm{mA}$ while varying I_{PA}. (b) Optical and (c) RF spectra of the MOPA in the same conditions.

the PA section when the MO current is fixed at $I_{MO} = 30\mathrm{mA}$ are shown in Fig. 2. This MO current corresponds to the DFB threshold for low and medium PA current [4]. At I_{PA} higher than 750 mA the power increases almost linearly, but soon it exhibits ripples and clear signs of thermal rollover. The ripples in the light-current characteristics of the MOPA are similar to those previously reported in 1060 nm MOPAs [5] and DBR tapered lasers [10], and they appear and disappear in a quasi-periodic way as I_{PA} is increased. In the present case, however, they involve wavelength jumps that were not observed in [5], [10]: as shown in Fig. 2(b), at the beginning of each ripple the

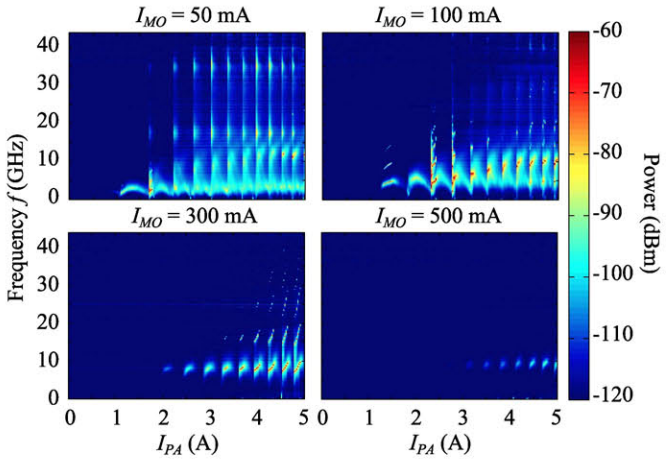

Fig. 3. Experimental characterization: RF spectra of the MOPA while varying I_{PA} for different I_{MO} values. I_{MO} = 50, 100, 300 and 500 mA.

emission wavelength of the MOPA jumps from that of the Bragg grating in the MO section ($\sim$1547 nm) to a much shorter one ($\sim$1530 nm) that corresponds to the gain peak of the material in the PA section. In this regime, the MOPA usually emits in several longitudinal modes, and the beat node at the mode spacing $\sim$17 GHz can be clearly observed in the RF spectrum.

If the current in the MO section is increased, the ripples of the P-I_{PA} characteristics become less visible and the large wavelength jumps do not occur anymore [4]. However at higher values of I_{MO} they are still apparent in the derivatives of the P-I curves, thus indicating a residual trend to transitions between different longitudinal modes. Fig. 3 shows the measured RF spectra as function of I_{PA} for different values of I_{MO}. A quasiperiodic behavior with I_{PA} is observed at all the MO injection levels. At $I_{MO} = 50$ mA, we observe the peaks at $\sim$17 GHz and high order harmonics arising from the beating of the complete cavity modes, alternating with peaks at frequencies between 5 and 10 GHz and with lower frequency peaks around 2–3 GHz. When increasing the MO current to 100 mA, the $\sim$17 GHz peaks disappear while the peaks between 5 and 10 GHz are stronger with high order harmonics. At $I_{MO} =$ 300 mA, the main RF peaks continue to be those between 5 and 10 GHz with a frequency which increases with the I_{PA} current. And finally, at $I_{MO} = 500$ mA the intensity of the RF peaks is still quasi-periodic but much lower, indicating a more stable emission.

III. Theoretical Modelling

In order to theoretically analyze the instability described in the previous section, we use the 1-D TWM developed in [8], [11] suitably modified in order to phenomenologically include the thermal drift of the material properties in each section. This TWM has been used in the past for studying similar wavelength jumps that occur in passively mode-locked semiconductor lasers [12], and it naturally includes multilongitudinal mode competition and coupled-cavity effects. We briefly summarize the model, and refer the reader to [11], [13], [14] for the details.

We consider a two-section device. Within each section j, an optical field with optical carrier frequency ω_0 and effective propagation constant q_0 is decomposed into a forward and a backward component which slowly-varying amplitudes, $E_j^{\pm}$, propagate according to

$$\pm\,\partial_z E_j^{\pm} + \frac{1}{v_j^g}\partial_t E_j^{\pm} = [i\delta_j(T_j) - \alpha_j^i]E_j^{\pm} + i\kappa_j^{\pm}E_j^{\mp} + iP_j^{\pm}, \tag{1}$$

where the field amplitudes and material variables have been suitably scaled [15], α_j^i is the (amplitude) absorption coefficient and v_j^g is the group velocity, that for the sake of simplicity are taken equal in both sections, i.e. $\alpha_i = \alpha_{MO}^i = \alpha_{PA}^i$ and $v_g = v_{MO}^g = v_{PA}^g$. $\kappa_j^{\pm}$ is the coupling coefficient of the Bragg grating in section j, if any. $\delta_j(T_j)$ is the thermally induced change of the effective index that induces an effective detuning with respect to ω_0 as a reference point. The detuning depends on the temperature of the section as

$$\delta_j(T_j) = \frac{\delta n_g}{\delta T}\frac{\Delta T_j}{L_j}, \tag{2}$$

where $\frac{\delta n_g}{\delta T}$ is the coefficient of thermal change in the effective group index.

Similarly, the total carrier density N_j is decomposed as $N_j(z,t) = N_j^0(z,t) + N_j^+ e^{2iq_0 z} + N_j^- e^{-2iq_0 z}$, where N_j^0 is the quasi-homogeneous component, $N_j^{\pm}$ (with $N_j^- = (N_j^+)^*$) are the spatial grating components arising from spatial-hole burning (SHB) due to the standing-wave effects in the section. These obey

$$\partial_t N_j^0 = \frac{I_j}{s_j} - R_j(N_j^0) - i(E_j^{+*}P_j^+ + E_j^{-*}P_j^- - c.c.) \tag{3}$$

and

$$\partial_t N_j^{\pm} = -[R_j'(N_j^0) + 4\mathcal{D}_j q_0^2]N_j^{\pm} - i(P_j^{\pm}E_j^{\mp *} - E_j^{\pm}P_j^{\mp *}), \tag{4}$$

where I_j is the current injected into the section (in A), s_j is a scale factor take into account the volume of the different sections, $R_j(N) = A_j N + B_j N^2 + C_j N^3$ is the carrier recombination rate in this section (which includes non-radiative, radiative and Auger recombination terms), $R_j'(N) = d_N R_j(N)$, $4\mathcal{D}_j q_0^2$ is the decay rate of the grating terms due to carrier diffusion, and the remaining terms describe stimulated recombination.

The polarization densities $P_j^{\pm}$, which describe the gain and carrier-induced refractive index, are given by

$$P_j^{\pm} = \chi_0 \int_0^{\infty} dt' \left\{ \chi_j[t', N_j^0(t', r)]E_j^{\pm}(z,r) + N_j^{\pm}(z,r)\frac{\partial \chi_j[t', N_j^0(r)]}{\partial N^j}E_j^{\mp}(z,r) \right\} + \eta\xi_j^{\pm}(z,t), \tag{5}$$

where $r = t - t'$. The convolution kernel $\chi(t,N)$ describes the optical response of the material in time domain under the intraband quasi-equilibrium approximation, which is valid on time scales of 1 ps and longer. We also add spontaneous emission of amplitude η by including a Gaussian white noise term $\xi_j^{\pm}(z,t)$ of zero mean and correlation $\langle \xi_j^{\pm}(z,t)\xi_j^{\pm}(\hat{z},\hat{t})\rangle = \delta(t-\hat{t})\delta(z-\hat{z})$. Although numerical approximations for $\chi(t,N)$ at finite

temperature have been developed [16], for computational simplicity here we shall use the analytical approximation developed for low-temperatures, which nevertheless provides a reasonable description of the material response at finite temperature [11]. In this approximation, the material response is expressed as

$$\chi_j(t', N_j) = e^{-[\gamma + i(\Omega_{Gj} - \omega_0)]t'} \frac{2e^{-i\gamma N_j t'} - 1 - e^{-i(\Omega_T - \Omega_{Gj})t'}}{t'}, \tag{6}$$

where γ is the decay rate of the material polarization, and Ω_{Gj} and Ω_T are the lowest and highest photon frequencies for the optical transitions.

In the simulations, each section provides its own gain and carrier-induced refractive index spectra as given by Eq. (6) depending on its bias point and temperature. As discussed below, the temperature dependence is included by considering that the band gap energy in each section varies linearly with temperature, and therefore the gain and index spectra for the whole device is the superposition of the detuned contribution for each section taking into account band-filling and thermal shift.

We describe phenomenologically the thermally induced redshift of the material gain peak considering

$$\Omega_{Gj} = \Omega_G^0 - c_j \Delta T_j, \tag{7}$$

this amounts to consider that the dominant temperature effect in both sections is to rigidly shift the optical response of the active material to longer wavelengths without changing its magnitude, which is acceptable if the temperature changes are not large.

The temperature in each section is phenomenologically described via self- and cross-heating coefficients [5]

$$\begin{pmatrix} \Delta T_{MO} \\ \Delta T_{PA} \end{pmatrix} = \begin{pmatrix} \theta_{11} & \theta_{12} \\ \theta_{21} & \theta_{22} \end{pmatrix} \begin{pmatrix} P_{MO} \\ P_{PA} \end{pmatrix} \tag{8}$$

where $P_{MO,PA}$ is the power dissipated within each section, $P_j = P_j^{elect} - P_j^{opt}$ with $P_j^{elect} = V_j I_j$, where $V_j = R_j I_j$. In practice, the output power is a function of the band-gap detuning that is a function of the temperature. The temperature is in turn a function of the difference between the injected electrical power but also the optical output of the device and it also evolves on a very slow time scale which renders the analysis very time consuming, see for instance [13]. However, we can simplify this complex feedback loop by noting that $1.5\,\mu$m devices have a low output efficiency, i.e., the optical power in each section is negligible as compared to the electrical power $P_j^{opt} \ll P_j^{elect}$. In addition, because even during the wavelength jumps the optical output power does not change appreciably, one can write $P_j^{opt} = a(P_j^{elect} - P_j^{th})$ meaning that apart from a irrelevant shift $P_j^{opt} = aP_j^{th}$ that can be absorbed into a redefinition of the equilibrium temperature, the dissipated power remains proportional to P_j^{elect}. In Eq. (8) the diagonal matrix elements θ_{jj} are the self-heating coefficients, and the non-diagonal ones describe cross-heating.

Finally, the TWM is closed by specifying the boundary conditions for the fields at the output facets ($z = 0, z_2$) and at the interface of the MO and the PA sections ($z = z_1$), as sketched in Fig. 4,

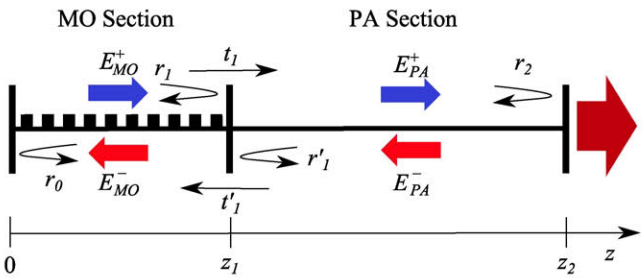

Fig. 4. Boundary conditions for the electrical fields $E^{\pm}_{MO}$ and $E^{\pm}_{PA}$ corresponding to each section of MOPA. r_0, r_1, r'_1, r_2 and t_1, t'_1 are the reflectivity and transmission coefficients for the fields amplitudes. $z_1 = L_{MO}$ and $z_2 = L_{MO} + L_{PA}$.

$$\begin{cases} E^+_{MO}(0,t) = r_0 E^-_{MO}(0,t) \\ E^-_{MO}(z_1,t) = r_1 E^+_{MO}(z_1,t) + t'_1 E^-_{PA}(z_1,t) \\ E^+_{PA}(z_1,t) = r'_1 E^-_{PA}(z_1,t) + t_1 E^+_{MO}(z_1,t) \\ E^-_{PA}(z_2,t) = r_2 E^+_{PA}(z_2,t) \end{cases} \tag{9}$$

where $z_1 = L_{MO}$ and $z_2 = L_{MO} + L_{PA}$. For a typical MOPA device, $r_2 \ll 1$ as appropriate for an AR-coated facet. Moreover, r_1 and r'_1 should also be small, and $t_1 \sim 1$ while $t'_1 < 1$ describe the weak coupling of the field from the PA section into the MO section and vice-versa due to the free-diffraction of the field in the PA section. Unless otherwise indicated, the parameters used are shown in Table I. We take the optical carrier wavelength as that corresponding to the Bragg wavelength in the MO section, i.e., $\lambda_{Bragg} = \lambda_0$. In order to simplify the analysis, we take $\Omega_{GMO} \simeq \Omega_G^0$ (i.e., $c_{MO} = 0$) because the redshift of the material peak at the MO section is small compared to that of the PA section as a consequence that in this paper we restrict ourselves to situations where I_{MO} is constant.

In summary, our TWM considers two separate sections with different temperatures and biasing points. Compound-cavity effects arise from the optical coupling of the MO and PA sections. Within each section, the local carrier density determines the gain and carrier-induced index spectra; the temperature of the section determines the local band gap energy and the effective index of the section. These two effects lead to changes in wavelength and net gain of the cavity modes when the bias currents are varied through self- and cross-heating.

A. Threshold Analysis

In order to get a more physical insight into the possible modal competition of our compound cavity device we perform the threshold analysis of Eqs. (1) and (3)–(5) in a similar way as we did previously [14] and detailed in Appendix A. The threshold analysis lead us to the following eigenvalue equation,

$$\begin{aligned} &(1 - r_0 r_m) e^{-\Lambda L_{MO}} \left[(1 - r_1 r_p) e^{\Xi L_{PA}} - p e^{-\Xi L_{PA}} \right] \\ &= (r_p - r_0) e^{\Lambda L_{MO}} \left[(r_m - r_1) e^{\Xi L_{PA}} - q e^{-\Xi L_{PA}} \right] \end{aligned} \tag{10}$$

where

$$p = t_1 t'_1 r_p r_2 + r'_1 r_2 (1 - r_1 r_p), \tag{11}$$

TABLE I
MODEL PARAMETERS

Symbol	Value	Units	Meaning
		Waveguide Parameters	
λ_0	1546.5	nm	Optical carrier wavelength
n_g	3.57	–	Effective group index
v_g	0.84×10^8	$\mathrm{m\,s^{-1}}$	Group velocity
L_{MO}	900	μm	Length MO section
L_{PA}	1600	μm	Length PA section
$2\alpha_i$	10	$\mathrm{cm^{-1}}$	Internal losses
r_0	$\sqrt{0.9}$	–	Reflection coeff. at $z = 0$
r_1	$\sqrt{10^{-6}}$	–	Reflection coeff. at $z = z_1$
t_1	$\sqrt{0.99}$	–	Transmission coeff. at $z = z_1$
r_1'	$\sqrt{10^{-7}}$	–	Reflection coeff. at $z = z_1$
t_1'	$\sqrt{0.1}$	–	Transmission coeff. at $z = z_1$
r_2	$\sqrt{10^{-4}}$	–	Reflection coeff. at $z = z_2$
κ	11.1	$\mathrm{cm^{-1}}$	Bragg coupling MO section
		Active Material Parameters	
N_t	2.2×10^{18}	$\mathrm{cm^{-3}}$	Transparency carrier density
$\mathcal{D}$	12	$\mathrm{cm^2\ s^{-1}}$	Ambipolar diffusion coeff.
A	0	$\mathrm{s^{-1}}$	Non radiative recombination
B	10^{-10}	$\mathrm{cm^3\ s^{-1}}$	Spontaneous recombination
C	7×10^{-29}	$\mathrm{cm^6\ s^{-1}}$	Auger recombination
$2\chi_0$	208	$\mathrm{cm^{-1}}$	Maximum modal gain
γ	39.2	THz	Polarization decay rate
Ω_G^0	0	GHz	Band-gap freq. at $T = 0$ K
Ω_T	392	THz	Top of the band frequency
η	1×10^{-5}	–	Spontaneous emission
		Thermal and Electrical Parameters	
$\delta n_g/\delta T$	10^{-4}	$\mathrm{K^{-1}}$	Temp. change n_g
c_{MO}	0	$\mathrm{THz\,K^{-1}}$	Band-gap redshift coeff. MO
c_{PA}	17	$\mathrm{THz\,K^{-1}}$	Band-gap redshift coeff. PA
θ_{11}	10	$\mathrm{K\,W^{-1}}$	Self-heating coeff. MO
θ_{22}	10^{-2}	$\mathrm{K\,W^{-1}}$	Self-heating coeff. PA
θ_{12}	1	$\mathrm{K\,W^{-1}}$	Cross-heating coeff. PA $\rightarrow$ MO
θ_{21}	10^{-6}	$\mathrm{K\,W^{-1}}$	Cross-heating coeff. MO $\rightarrow$ PA
R_{MO}	3	Ω	Electrical resistance MO
R_{PA}	3	Ω	Electrical resistance PA
s_{MO}	4.6×10^{-11}	A	Current scale factor MO
s_{PA}	8.1×10^{-10}	A	Current scale factor PA

$$q = t_1' t_1 r_2 + r_1' r_2 (r_m - r_1), \tag{12}$$

$$\Lambda^2 = (\lambda/v_g + \alpha_i + i\delta_{MO} - i\tilde{\chi}_{MO}^{\lambda})^2 + |\kappa|^2, \tag{13}$$

$$\Xi = \lambda/v_g + \alpha_i + i\delta_{PA} - i\tilde{\chi}_{PA}^{\lambda}. \tag{14}$$

which has to be solved for eigenvalue $\lambda = i\Omega_m$, being Ω_m the modal frequencies. In addition it depends on two parameters: the uniform carrier densities in each section, N_{MO}^0 and N_{PA}^0, determined through $I_j = s_j R(N_j^0)$. We first determine the threshold of the MO section considering the full structure with a carrier density in the PA section fixed to zero.

Fig. 5(a) displays the modal thresholds for $\kappa L_{MO} = 0.5$, 1 and 2; with the carrier density in the PA section, $N_{PA}^0 = 0$. We can see that the threshold properties of the device depend noticeably on κ and the carrier density in the PA section. For a moderate value of $\kappa L_{MO} = 1$ (i.e., $\kappa = 11.1\,\mathrm{cm^{-1}}$) and $N_{PA}^0 = 0$, the threshold of the device occurs close to the Bragg frequency at moderate values of the $N_{MO}^0 = 1.3$ ($I_{MO}^{Th} = 49$ mA). We can see the effect of the stop-band of the Bragg grating in Fig. 5(b) where the frequency difference between contiguous modes Δf is shown. For $\kappa L_{MO} = 2$ we see a maximum $\Delta f = 87$ GHz, and $\Delta f = 65$ and 63 GHz for $\kappa L_{MO} = 1$ and 0.5

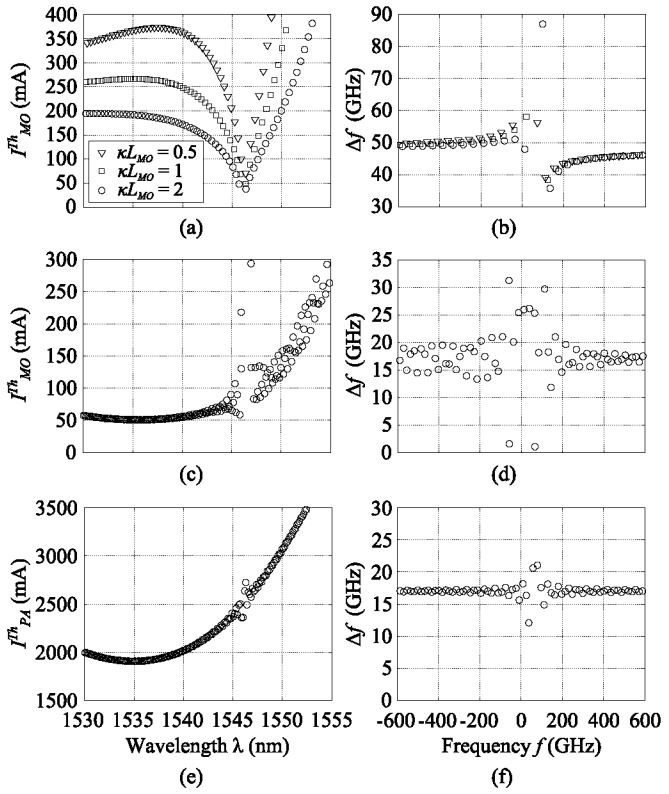

Fig. 5. Left column: Modal threshold. Right column: Frequency difference Δf between contiguous modes. (a) and (b): Current threshold of the MO section I_{MO}^{Th} for $\kappa L_{MO} = 0.5$, 1 and 2 with $N_{PA}^0 = 0$. (c) and (d): Current threshold of the MO section I_{MO}^{Th} for $\kappa L_{MO} = 1$ with $N_{PA}^0 = 1.5$. (e) and (f): Current threshold of the PA section I_{PA}^{Th} for $\kappa L_{MO} = 1$ with $N_{MO}^0 = 1$.

respectively. We notice that as expected the effect of the Bragg grating modifies the free spectral range (FSR) of the MO section ($\mathrm{FSR}_{MO} \sim 47$ GHz) nearby the Bragg frequency. In these conditions, however, the unpumped PA absorbs the light emitted by the MO and no useful output is obtained.

The PA section must then be pumped, but this may induce a strong change in the threshold properties of the device. On one side, the effective reflectivity experienced by the MO will change due to the double passage of light in the PA section. On the other, the gain peak of the PA section will not in general occur close to the Bragg frequency due to the blue shift induced by band filling and to the red shift induced by heating of the material. As shown in Fig. 5(c), when the PA section is pumped such that $N_{PA}^0 = 1.5$, the gain peak of the PA section is located around $\lambda = 1535$ nm, i.e., strongly blue-detuned with respect to the Bragg wavelength, while the gain peak of the MO section is close to λ_{Bragg}. As a consequence, the threshold of the MO now occurs around 1535 nm for a carrier density in the MO section which is $N_{MO}^0 = 1.3$ ($I_{MO}^{Th} \sim 50$ mA). In addition, close to threshold the device will display a rather different modal structure in the two cases. In the former case, i.e., no amplification in the PA, the frequency spacing of the modes corresponds to that of the FSR_{MO}, and it is not regular due to the dispersion of the Bragg mirror. In the latter, instead, more modes arise as a consequence of compound cavity effects with additional modulations that are quite regularly spaced with a

mode spacing that corresponds to the full length of the cavity, $\mathrm{FSR}_{MOPA} \sim 17$ GHz (see Fig. 5(d)). Remark, however, that for frequencies close to 0 (i.e., close to the Bragg wavelength), the modal structure is quite irregular, with mode spacings that do not correspond to any clear section. The reason is that in these conditions, the effective reflectivity of the output facet can be quite substantial. The induced strong coupled-cavity effects lead to a strong modulation of the intermode spacing, that can be as low as a few GHz. Such a small intermode spacing might couple with the ROs in the carrier density, leading to instabilities in the dynamical behavior of the device. As shown in Fig. 5(e) and (f), similar results (at higher threshold currents) are found when fixing $N^0_{MO} = 1$ and solving Eq. (10) for Ω_m and N^0_{PA} (I^{Th}_{PA}). Stronger values of κ mitigate such a behavior, because a larger carrier density in the PA section is needed to make the threshold jump from the Bragg wavelength to that of the gain peak in the PA section. However, the instabilities can always occur for high-enough currents in the PA section, because the threshold of the MO saturates as κ increases.

IV. Above Threshold Characteristics

The former discussion about the threshold properties of the device indicates that the wavelength jumps may occur when the gain peak of the PA is high enough, but the analysis lacks nonlinear effects hence it is not appropriate to describe the behavior of the device above threshold, where the carrier density may develop a non-uniform profile due to the interaction with the optical field. In addition, the thermal drift of the material properties as the currents are increased may also change the stability properties of the optical solutions. For these reasons, assessing the properties of the device above threshold requires the numerical integration of the full TWM. In our case this is performed via the numerical algorithm developed in [17], that has already been successfully applied to the study of several semiconductor laser systems [8], [12]–[14] and which allows us to explore the impact that the different device parameters have on the dynamics. The numerical algorithm used to solve the full TWM can be found in [15]. We have used a spatial discretization of $\widetilde{N}_{MO} = 1491$ points and $\widetilde{N}_{PA} = 2651$ points for each section (corresponding to a time step $\Delta t = 7.2$ fs) with a decimation factor $D = 10$ and the convolution kernels are computed using $M = 22$ points in the past. Using a standard PC (Intel Core i7 4790K at 4.4 GHz with 32 Gb RAM) a simulation of 10 ns parallelized in 4 cores takes 220 s to be completed. The following results have been obtained by performing 300 simulations, the previous system state has been used as the starting point of the next one while increasing I_{PA}.

Fig. 6 displays the power-current characteristics, and the optical and RF spectra of the MOPA for the parameters given in Table I in the case of a moderate value of $\kappa L_{MO} = 1$ (i.e., $\kappa = 11.1\,\mathrm{cm}^{-1}$) when I_{PA} is scanned and the current in the MO section is kept constant, $I_{MO} = 54\,\mathrm{mA}$. The MOPA threshold occurs for $I_{PA} \sim 1$A, and the lasing wavelength corresponds to that of the Bragg grating in the MO section. As the current in the PA section is increased, the optical power emitted by the device increases almost linearly, and the emission wavelength exhibits

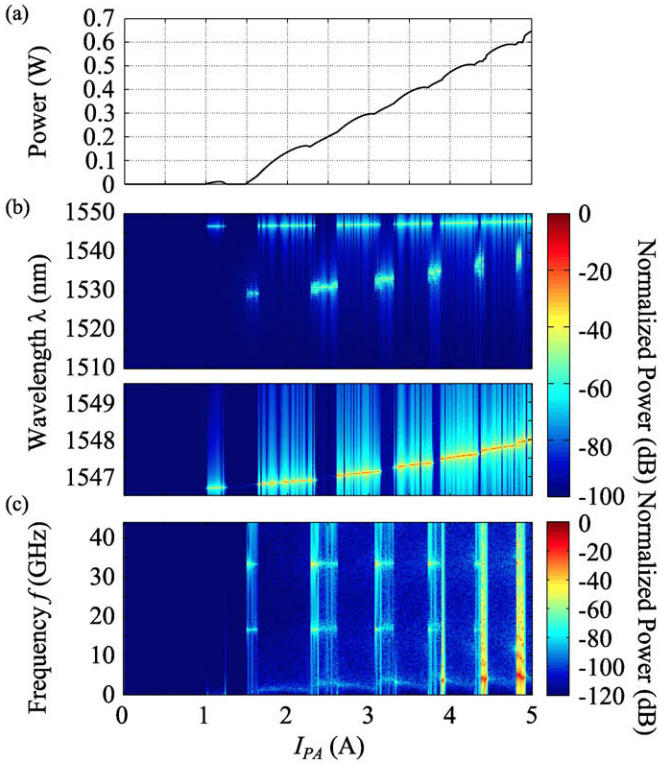

Fig. 6. Theoretical results: (a) P-I characteristics for $I_{MO} = 54\,\mathrm{mA}$ while varying I_{PA}. (b) Optical and (c) RF spectra of the MOPA in the same conditions.

a small redshift due to the thermal drift of the Bragg wavelength as the refractive indexes increase due to cross-heating. However, increasing the current in the PA section soon leads to a ripple in the power-current characteristics similar to those observed in Fig. 2(a) at low currents of the PA section (at $I_{PA} = 1.2$ and 1.8 A). Nevertheless, the ripples in the numerical simulations always occur downwards, while in the experiment the ripples at high PA current are upwards. We note that the sense of the ripples is determined by the net gain spectrum, which depends on the total losses at the operation wavelength. In the numerical simulations, several parameters ($r_0, r_1, r'_1, t_1, t'_1, r_2, \kappa$, etc.) determine the loss spectrum in the complete cavity, and the chosen values may not perfectly match those in the experiment.

At each ripple, the optical spectrum of the device changes dramatically, passing from narrow emission at the Bragg wavelength to broadband emission at a much shorter wavelength that corresponds to that of the material gain peak in the PA section. In this regime, the RF spectrum displays strong peaks at $f = 17\,\mathrm{GHz}$ and 34 GHz, which corresponds to the FSR_{MOPA}. Additional peaks at lower frequencies (between $f = 1.6$–$3\,\mathrm{GHz}$) can also be observed (see Fig. 5(c)), possibly enhanced by their coupling through the ROs. Further increasing the PA current additional peaks at low frequencies appear. The evolution of these low frequency peaks as I_{PA} increases follows the quasi-periodic jumps, in that regions the peaks increase their frequency (and produce high order harmonics for high I_{PA}); while in the regions where the Bragg wavelength dominates, their frequency diminishes. The phenomena is also observed in the experiments, see Fig. 2(c).

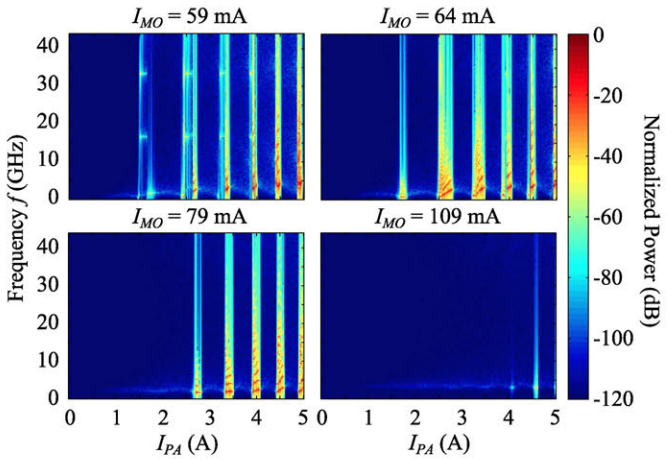

Fig. 7. Theoretical results: RF spectra of the MOPA while varying I_{PA} for different I_{MO} values. I_{MO} = 59, 64, 79 and 109 mA.

The large wavelength jumps described above occur in a quasi-periodic way upon increasing the PA current provided that I_{MO} is low. As I_{MO} is increased, the ripples in the P-I_{PA} curve become less visible (not shown) and changes in the RF spectra are obtained, see Fig. 7. For $I_{MO} = 59$ mA traces of the modes of the full MOPA cavity are still visible at intermediate values of I_{PA}, together with peaks at lower frequencies. These low frequency peaks dominate the RF spectrum for higher values of I_{PA}, their frequency increasing with I_{PA} in this regime. For higher I_{MO} currents, the modes of the full MOPA cavity disappear and only these peaks at low frequency behave in a quasi-periodic way upon increasing I_{PA} (see Fig. 7, $I_{MO} = 64$ and 79 mA). For $I_{MO} = 109$ mA the RF peaks are less visible indicating that stable emission has been achieved. These results are in agreement with those obtained from the experiments, see Fig. 3. We interpret these peaks at low frequency as an undamping of the carrier density ROs. When the gain peak at the PA section is not sufficiently high to lase itself and it may enhances the coupling to the carrier density ROs of additional modes appearing close to λ_{Bragg} arising as a consequence of the compound cavity effects and the Bragg grating (in similar way as shown in Fig. 5(d)).

The main physical mechanism at the root of these behaviors is the drift of the cavity modes over the modulated loss spectrum created by the compound cavity effects arising from the effective reflectivity of the output facet, i.e., including amplification and back-coupling. The amplitude of the modulation of the cavity losses depends on several parameters (r_0, r_1, r_1', t_1, t_1', r_2, κ, etc.); in particular, t_1' and r_2 determine the back-coupling of the light from the PA to the MO. On the other hand, the precise wavelength of the cavity modes depends on the effective and carrier-induced index change in each section. Temperature changes arising from self- and cross-heating will lead to modal drifts that change the net modal gain. Therefore, even though the bias of the MO section is kept constant, variations of the net gain close to the Bragg wavelength occur when the PA bias is changed. When the MO section is biased close to its threshold, the net modal gain at Bragg wavelength is small, see Fig. 5(c), and a small drift of the modes close to the λ_{Bragg} might promote the emission at wavelengths close to the gain peak of the PA section. Conversely when the mode close to λ_{Bragg} approaches the local minimum of losses, emission at λ_{Bragg} is recovered. Instead, when the MO section is biased above its threshold, the emission at the Bragg wavelength is preferred and the modal changes do not promote the emission at the gain peak of the PA section but disturb the dynamics by enhancing low frequency peaks observed in the RF spectrum that may be attributed to a coupling with the ROs. The above explanation is confirmed by the numerical observation that if the cross-coupling coefficient is reduced to $\theta_{12} = 0.1$ K W^{-1}, the MOPA emits stably at the Bragg wavelength for all the range of I_{PA} scanned at all current values of the MO section. The P-I curve shows no ripples, and the optical spectrum displays stable emission at λ_{Bragg} without any trace of jumps. Besides, our simulations show that the tendency to jump in wavelength is reduced by increasing the net gain close to λ_{Bragg}, which can be accomplished by increasing either κ or r_0.

The quasi-periodic occurrence of these jumps is a consequence of the 2π-periodic nature of the cavity modes. If the mechanisms of modal drift were all known, the currents where wavelength jumps occur could be determined similarly to [5]. In our case, however, the complex interplay of thermal and carrier-induced mechanisms of modal drift make this task highly complicated, and a linear stability analysis of the full TWM [14] is required in order to address this question.

V. Conclusion

We have theoretically analyzed the large wavelength jumps that are observed in the emission wavelength of some monolithically integrated master oscillator power amplifiers emitting at 1.5 μm as the current in the PA section is increased. The 1-D TWM used successfully reproduces the observed behavior, and it confirms that the instabilities observed occur through longitudinal mode competition, with beam filamentation playing no relevant role. The TWM allows to trace the origin of these instabilities back to the drift of the cavity modes over the compound-cavity losses due to cross-heating of the MO section as the current in the PA section is varied. The anomalous peaks that appear in the RF spectrum in both the experiment and the numerical simulations can be explained by the threshold analysis of the MOPA as arising from the undamping of the ROs caused by the coupling of the compound cavity modes. Moreover, our numerical simulations indicate that minimizing the cross-heating from the PA to MO section leads to a more stable emission. Alternatively, increasing the value of κ or r_0 can also mitigate these instabilities. However, a detailed and deeper analysis of the different mechanisms involved is still required and will be the subject of further investigation.

Appendix A
Threshold Analysis

The TWM described in Eqs. (1) and (3)–(5) admits a trivial solution $E_j^{\pm} = P_j^{\pm} = N_j^{\pm} = 0$ and $I_j = s_j R(N_0^{sj})$ where no optical power is emitted. The threshold of the MOPA corresponds to the lowest operation point that renders this off-solution

unstable, hence for currents above it, any fluctuation in the optical field will be amplified and the system will start lasing.

The threshold of the MOPA can be thus determined by performing the linear stability analysis of this off-solution. By considering small perturbations to the off-solution,

$$\begin{cases} E_j^{\pm}(z,t) = a_j^{\pm}(z,t) \\ P_j^{\pm}(z,t) = p_j^{\pm}(z,t) \\ N_j^0(z,t) = N_0^{sj} + n_j^0(z,t) \\ N_j^{\pm}(z,t) = n_j^{\pm}(z,t) \end{cases}, \tag{15}$$

the linearized TWM equations read

$$\pm\,\partial_z a_j^{\pm} = -\frac{1}{v_j^g}\partial_t a_j^{\pm} - \alpha_j^i a_j^{\pm} + i p_j^{\pm} - i\kappa_j^{\pm} a_j^{\mp} \tag{16}$$

$$p_j^{\pm} = \chi_0 \int_0^{\infty} dt' \chi_j(t', N_0^{sj}) a_j^{\pm}(z, t-t') \tag{17}$$

and

$$\partial n_j^0 = -R'(N_j^0) n_j^0 \tag{18}$$

$$\partial_t n_j^{\pm} = -[R'(N_j^0) + 4\mathcal{D}q_0^2] n_j^{\pm}. \tag{19}$$

The equations for the perturbations in the carrier density decouple from those for the field, and they are both unconditionally stable. It is therefore enough to consider the field equations in order to determine the stability of the off-solution. The temporal dependence can be removed by considering

$$a_j^{\pm}(z,t) = a_j^{\pm}(z) e^{\lambda t}. \tag{20}$$

Solutions with $Re(\lambda_j) > 0$ corresponds to unstable solutions and vice-versa, and the crossing point determines the modal threshold and frequency. Then, the field equations within each section read

$$\begin{cases} \partial_z a_j^+ = -(\lambda/v_j^g + \alpha_j^i - i\tilde{\chi}_j^{\lambda}) a_j^+ - i\kappa_j^+ a_j^- \\ \partial_z a_j^- = (\lambda/v_j^g + \alpha_j^i - i\tilde{\chi}_j^{\lambda}) a_j^- + i\kappa_j^- a_j^+ \end{cases}, \tag{21}$$

where

$$\tilde{\chi}_j^{\lambda} = \chi_j^0 \int_0^{\infty} \chi_j(t', N_j^0) e^{-\lambda t'} dt'. \tag{22}$$

In the MO section, $\kappa_{MO}^+ \equiv \kappa$, $\kappa_{MO}^- \equiv \kappa^*$, and then the solution for Eq. (21) can be written as

$$\begin{cases} a_{MO}^+(z) = a_1 e^{\Lambda z} + r_p b_2 e^{-\Lambda z} \\ a_{MO}^-(z) = r_m a_1 e^{\Lambda z} + b_2 e^{-\Lambda z} \end{cases}, \text{ for } 0 \le z \le z_1, \tag{23}$$

where we have defined

$$\Lambda^2 = \left(\frac{\lambda}{v_{MO}^g} + \alpha_{MO}^i + i\delta_{MO} - i\tilde{\chi}_{MO}^{\lambda}\right)^2 + |\kappa|^2 \equiv \xi^2 + |\kappa|^2, \tag{24}$$

$$r_p = \frac{i\kappa}{\Lambda - \xi}, \quad r_m = \frac{i\kappa^*}{\Lambda - \xi}. \tag{25}$$

For the PA section, $\kappa_{\pm}^{PA} = 0$, the system Eq. (21) is not coupled and the solution can be written as

$$\begin{cases} a_{PA}^+(z) = c_1 e^{-\Xi(z-z_1)} \\ a_{PA}^-(z) = c_2 e^{\Xi(z-z_1)} \end{cases}, \text{ for } z_1 \le z \le z_2, \tag{26}$$

where

$$\Xi = \frac{\lambda}{v_{PA}^g} + \alpha_{PA}^i + i\delta_{PA} - i\tilde{\chi}_{PA}^{\lambda}. \tag{27}$$

Imposing the boundary conditions to the solutions leads to the eigenvalue equation (Eq. (10) in the main text.)

$$\begin{aligned} &(1 - r_0 r_m) e^{-\Lambda L_{MO}} \left[(1 - r_1 r_p) e^{\Xi L_{PA}} - p e^{-\Xi L_{PA}}\right] \\ &(r_p - r_0) e^{\Lambda L_{MO}} \left[(r_m - r_1) e^{\Xi L_{PA}} - q e^{-\Xi L_{PA}}\right] \end{aligned} \tag{28}$$

where

$$p = t_1 t_1' r_p r_2 + r_1' r_2 (1 - r_1 r_p), \tag{29}$$

$$q = t_1' t_1 r_2 + r_1' r_2 (r_m - r_1). \tag{30}$$

and we have used that $z_1 = L_{MO}$ and $z_2 = L_{MO} + L_{PA}$. The eigenvalue equation is equivalent to that found in simpler device configurations. Indeed, if one sets $r_2 = 0$, the well-known eigenvalue equation for a DFB, is recovered as expected: if the output facet reflectivity is strictly zero, the device threshold is that of the MO section regardless of the state of the PA section, which only provides gain. In addition, setting $t_1' = 0$ (the MO is decoupled from the PA) factorizes the eigenvalue equation where the first factor provides the eigenvalues of the MO and the second one those of the PA Fabry-Pérot structure. The lasing threshold then corresponds to the lowest threshold of either device.

REFERENCES

[1] H. Wenzel *et al.*, "High peak power optical pulses generated with a monolithic master-oscillator power amplifier," *Opt. Lett.*, vol. 37, no. 11, pp. 1826–1828, Jun. 2012.

[2] P. Adamiec *et al.*, "High-peak-power pulse generation from a monolithic master oscillator power amplifier at 1.5 μm," *Appl. Opt.*, vol. 51, no. 30, pp. 7160–7164, Oct. 2012.

[3] M. Wright and D. Bossert, "Temporal dynamics and facet coating requirements of monolithic MOPA semiconductor lasers," *IEEE Photon. Technol. Lett.*, vol. 10, no. 4, pp. 504–506, Apr. 1998.

[4] M. Vilera *et al.*, "Emission characteristics of a 1.5 μm all semiconductor tapered master oscillator power amplifier," *IEEE Photon. J.*, vol. 7, no. 2, p. 1500709, Apr. 2015.

[5] M. Spreemann *et al.*, "Measurement and simulation of distributed-feedback tapered master-oscillators power-amplifiers," *IEEE J. Quantum Electron.*, vol. 45, no. 6, pp. 609–616, Jun. 2009.

[6] A. Egan *et al.*, "Dynamic instabilities in master oscillator power amplifier semiconductor lasers," *IEEE J. Quantum Electron.*, vol. 34, no. 1, pp. 166–170, Jan. 1998.

[7] M. Radziunas *et al.*, "Mode transitions in distributed-feedback tapered master-oscillator power-amplifier: Theory and experiments," *Opt. Quantum Electron.*, vol. 40, no. 14–15, pp. 1103–1109, 2008.

[8] J. Javaloyes and S. Balle, "Emission directionality of semiconductor ring lasers: A traveling-wave description," *IEEE J. Quantum Electron.*, vol. 45, no. 5, pp. 431–438, May 2009.

[9] A. Pérez-Serrano, J. Javaloyes, and S. Balle, "Spectral delay algebraic equation approach to broad area laser diodes," *IEEE J. Sel. Topics Quantum Electron.*, vol. 19, no. 5, pp. 1–8, Sep. 2013.

[10] K.-H. Hasler *et al.*, "5-W DBR tapered lasers emitting at 1060 nm with a narrow spectral linewidth and a nearly diffraction-limited beam quality," *IEEE Photon. Technol. Lett.*, vol. 20, no. 19, pp. 1648–1650, Oct. 2008.

[11] J. Javaloyes and S. Balle, "Quasiequilibrium time-domain susceptibility of semiconductor quantum wells," *Phys. Rev. A*, vol. 81, no. 6, p. 062505, Jun. 2010.
[12] P. Stolarz *et al.*, "Spectral dynamical behavior in passively mode-locked semiconductor lasers," *IEEE Photon. J.*, vol. 3, no. 6, pp. 1067–1082, Dec. 2011.
[13] G. Tandoi *et al.*, "Subpicosecond colliding pulse mode locking at 126 GHz in monolithic GaAs/AlGaAs quantum well lasers: Experiments and theory," *IEEE J. Sel. Topics Quantum Electron.*, vol. 19, no. 4, pp. 1 100 608–1 100 608, Jul. 2013.
[14] A. Pérez-Serrano, J. Javaloyes, and S. Balle, "Directional reversals and multimode dynamics in semiconductor ring lasers," *Phys. Rev. A*, vol. 89, p. 023818, Feb. 2014.
[15] J. Javaloyes and S. Balle. (2012). *Freetwm: A Simulation Tool for Semiconductor Lasers*. [Online]. Available: http://onl.uib.es/es/Softwares/Freetwm/
[16] J. Javaloyes and S. Balle, "Detuning and thermal effects on the dynamics of passively mode-locked quantum-well lasers," *IEEE J. Quantum Electron.*, vol. 48, no. 12, pp. 1519–1526, Dec. 2012.
[17] J. Javaloyes and S. Balle, "Multimode dynamics in bidirectional laser cavities by folding space into time delay," *Opt. Exp.*, vol. 20, no. 8, pp. 8496–8502, Apr. 2012.

Antonio Pérez-Serrano was born in Badalona, Spain, in 1978. He received the Graduate degree in physics and the Ph.D. degree in physics from the Universitat de les Illes Balears, Palma de Mallorca, Spain. After a postdoc at the Weierstrass Institute, Berlin, he is currently a Research Associate at the Universidad Politécnica de Madrid, Spain. His research interests include semiconductor laser modeling and dynamics, with particular emphasis in multimode dynamics, ring lasers, multisection lasers and high-power broad area lasers.

Mariafernanda Vilera was born in Calabozo, Venezuela, in 1985. She received the M.Sc. degree in telecommunication engineering from Universidad Carlos III de Madrid, Madrid, Spain, in 2009. Since 2012, she has been working toward the Ph.D. degree at Universidad Politécnica de Madrid. Her research interests include high-brightness semiconductor lasers and laser sources for space applications.

Julien Javaloyes was born in Antibes, France, in 1977. He received the M.Sc. degree in physics from the ENS Lyon and the Ph.D. degree in physics from the Institut Non Linéaire de Nice/Université de Nice Sophia-Antipolis working on recoil induced instabilities and self-organization processes in cold atoms. He worked on delay-induced dynamics in coupled semiconductor lasers, VCSEL polarization dynamics, and monolithic mode-locked semiconductor lasers. He joined the Physics Department, Universitat de les Illes Balears as a Ramón y Cajal Fellow in 2010. His research interests include laser dynamics and bifurcation analysis.

Jose Manuel G. Tijero was born in Burgos, Spain, in 1960. He received the M.Sc. and Ph.D. degrees in physics from the University of Zaragoza, Zaragoza, Spain, in 1984 and from the Autonomous University of Madrid, Madrid, Spain, in 1989, respectively. Following a postdoctoral stay at the Electrical Engineering Department, University of California, Los Angeles (1990–1992) he became an Associate Professor at the Polytechnical University of Madrid in 1994. His research activity has included the spectroscopic study of defects in ionic crystals, the optoelectronic characterization of SiGe/Si heterostructures, and the study of InGaAs/GaAs lasers and quantum well infrared detectors. His current research interests include the modeling, simulation, and characterization of laser diodes for high-power applications.

Ignacio Esquivias was born in Madrid, Spain, in 1955. He received the M.Sc. and Ph.D. degrees in electronic engineering from the Universidad Politécnica de Madrid, Madrid, Spain, in 1977 and 1983, respectively, becoming a Full Professor at this university in 2001. He leads the Laser Diode Group of the CEMDATIC, with activity in laser diode modeling and characterization since 1992. He has been PI in ten national and five EC funded international projects on laser diodes, and he has published more than 100 journal and conference papers on this field. He coordinates the EC funded project BRITESPACE.

Salvador Balle (M'92) was born in Manacor, Mallorca. He received the Graduate degree in physics from the Universitat Autònoma de Barcelona, Barcelona, Spain, where he received the Ph.D. degree in physics on the electronic structure of strongly correlated Fermi liquids. After postdoctoral stages in Palma de Mallorca and Philadelphia where he became interested in stochastic processes and Laser dynamics, he joined in 1994 the Physics Department of the Universitat de les Illes Balears, where he is a Professor of optics since 2006. His research interests include laser dynamics, semiconductor optical response modeling, multiple phase fluid dynamics, and laser ablation phenomena.